Received: 23 May 2019 | Revised: 23 August 2019 | Accepted: 14 September 2019

DOI: 10.1002/aic.16816

AIChE JOURNAL

SEPARATIONS: MATERIALS, DEVICES AND PROCESSES

Core–shell adsorbents by electrospun MOF-polymer composites with improved adsorption properties: Theory and experiments

Mitchell R. Armstrong | Bohan Shan | Joseph Winarta | Bin Mu

Chemical Engineering, School for Engineering of Matter, Transport, and Energy, Arizona State University, Tempe, Arizona

Correspondence
Bin Mu, Chemical Engineering, School for Engineering of Matter, Transport, and Energy, Arizona State University, 501 East Tyler Mall, Tempe, AZ.
Email: bmu@asu.edu.

Funding information
Division of Chemical, Bioengineering, Environmental, and Transport Systems, Grant/Award Number: 1748641; Division of Civil, Mechanical and Manufacturing Innovation, Grant/Award Number: 1825594

Abstract

A new class of core–shell adsorbents has been created by electrospun metal–organic framework (MOF) particles embedded in polymer nanofibers, which have provided many unique properties compared to the existing MOF coating technologies. For the first time, we demonstrate the improved adsorption selectivity of CO_2 over N_2 using electrospun polymer/ZIF-8 adsorbents in experiments. Furthermore, an analytical model based on the assumption that the diffusivity in core is 10 times higher than that in shell is developed to describe the theory of improved selectivity for core–shell adsorbents that is validated against a more accurate finite element model developed in COMSOL. Our model shows three regimes including exclusive shell uptake, linear core uptake, and asymptotic core uptake. These regimes are related to material properties and uptake times, which could be used as design criteria to balance core stability, maximum selectivity, and maximum uptake. An advanced HAADF STEM tomography (Movie S1) shows that the shell thickness in the case of polymer/ZIF-8 is on the order of 10 nm, allowing the regime of maximum selectivity to be realized. Kinetically limited adsorption tests at 45°C demonstrate that these composite fibers can perform in a regime of selectivity and uptake for the separation of CO_2 and N_2 that is unobtainable by either the MOF or fiber independently, showing a great potential for postcombustion CO_2 capture.

KEYWORDS
core–shell structure, adsorption/gas, metal–organic frameworks, composite adsorbent, electrospun nanofiber nanoparticle composites

1 | INTRODUCTION

Since 1989, metal–organic-frameworks (MOFs) have been touted as a promising material that may be tailor-made for a variety of chemical selective applications including separation and catalysis.[1-5] The theoretically infinite combination of metal nodes and ligands allows for the rational design of active sites, pore networks, and surface area.[6,7] While some industrial applications have emerged as we see in the ION-X gas storage cylinder developed by NuMat Technologies,[8] the extensive use of MOFs is still limited. This is primarily due to both expensive synthesis costs of the more complex ligand structures and a lack of stability among a high percentage of MOFs.[9] These stability issues arise from the traditionally weak coordination bonding environments between metal and ligand, prohibiting most of these structures from surviving actual chemical environments,[10] although some Zirconium and Group 4 metal-based MOFs have relatively higher stability.[11-13]

Postcombustion carbon capture is an example of an application that promising and affordable MOFs are not stable enough to make an impact. For an adsorbent to be used for postcombustion carbon capture, it must exhibit great stability, high CO_2 uptake at 1 bar above

40°C and reasonably reject N_2 adsorption to minimize the energy penalty of regeneration.[14] Many materials have been examined for the carbon capture application including porous carbons, zeolites, polymers, and MOFs.[15-18] Although some MOFs demonstrate superior performance in CO_2 uptake, including MgMOF-74 with a CO_2 capacity of 8.61 mmol/g,[19] these same MOFs lack water stability and N_2 rejection. Strategies to increase selectivity and/or attenuate water uptake by forming a protective shell on the external surfaces of a MOF core are emerging, and a survey of these techniques is given in Table 1.

These studies show that widespread implementation of MOF adsorbents in a core–shell structure containing a highly selective nano-dimensional shell surrounding a MOF core may be feasible if this barrier is able to provide enhanced protection and increased selectivity. This could be through either a molecular sieving or solution-diffusion bottlenecking mechanism, yet allow desirable molecules to pass through the barrier over acceptable timescales.

When designing core–shell adsorbents, the shell must be thin enough to allow the desirable adsorbate to reach the core in a reasonable time. Even micrometer thick polymer shells have been shown to slow adsorption kinetics enough to effectively block nearly all adsorption in some cases.[22] Along with those mentioned previously, one enabling technology for reproducibly creating nanometer scale polymer coatings over MOFs is electrospinning.[30,32,33] Electrospun MOF composites have previously been created using highly permeable polymers with high MOF loadings, and shown to have high MOF accessibility.[28-30,34,35] Through the selection of highly selective polymers rather than highly permeable polymers, enhanced rejection of either water or undesirable gases may be realized. Furthermore, due to a single macroscopic dimension along the length of the fiber, these composites are readily processable and come preshaped for adaptation into adsorption columns. Electrospun fibers—with inherently high porosity, surface area, and aspect ratios—offer desirable features for a material to be used in adsorption columns.[36] Also, the fact that nearly all soluble polymers may be used for electrospinning allows a near-infinite choice in polymers selection to be pursued for designing optimum adsorbent composites. In fact, an entire field is emerging for the design of new polymer systems specifically for electrospinning including block-copolymers ionomers,[37] biopolymers,[38] and polymer blends.[39] Postsynthetic treatment of electrospun fibers such as crystallization, cross-linking, and inducing porosity have also proven to be viable tools for manipulating the fiber properties.[34,35,40]

Coating MOFs with electrospun polymer barriers allows selectivity and stability requirements for the adsorbent composite to be decoupled from the MOF design, enabling a rational design process for meeting industrial requirements. The idea of creating adsorbents that separate gases based on kinetic selectivity rather than thermodynamic selectivity is not new[41]; using selectivity in zeolites based on molecular sieving has been studied for some time.[42] However, introducing the solution-

TABLE 1 Survey of core–shell MOF composites in literature

Method	Shell	MOF core	Comments
Solvothermal secondary growth	Bio-MOF-14	Bio-MOF-11	Selectivity/capacity properties greater than either individual MOF for CO_2/N_2 adsorption, some water protection[20]
Epitaxial secondary growth	$Zn(ADC)_2$	$Zn(BDC)_2$	Selectivity/capacity properties greater than either individual MOF for cetane/isocetane liquid separation[21]
Spray drying microspheres	PS	HKUST-1	Tradeoff between water protection and accessibility based on loading/thickness[22]
Bath sonication	Organosilicone	ZIF-67 HKUST-1 NH_2-MIL-125	Coating method that increases water resistance that may be applied to many MOFs[23]
Silicone vapor deposition	PDMS	MOF-5 ZnBT HKUST-1	Water protection observed both surface area and crystallinity of MOF was preserved after coating.[24]
Polymer coating	Silica	ZrMOF	Water protection observed in a process too intense for most MOFs[25]
Shell ligand-exchange	DMBIM	ZIF-8	Ligands on outer layers of the MOF are exchanged to form a shell, promoting water resistance[26]
Heat-treatment	Carbon-coating	MOF-5	Enhanced moisture resistance[27]
Electrospinning	PAN	HKUST-1	Up to 80% loading and full accessibility by N_2 at 77 K[28]
Electrospinning	PVP	ZIF-8	MOF inside fibers and full accessibility by N_2 at 77 K[29]
Electrospinning	PEO	ZIF-8	Embedded MOFs are covered and negligible N_2 uptake in MOF observed in dilute loading regime at 77 K[30]
Electrospinning	PS	HKUST-1	Prolonged CO_2 adsorption capacity after hydrothermal exposure[31]

Abbreviations: DMBIM, dimethylbenzeimmidazole; PAN, poly(acrylonitrile); PDMS, polydimethylsiloxane; PEO, poly(ethylene oxide); PS, polystyrene; PVA, poly(vinyl alcohol); PVP, poly(vinylpyrridine).

diffusion mechanism from membrane permeance over adsorbent particles for separation applications is still new and not well understood for separation applications. Previous works have alluded to this mechanism, or mentioned its presence for both enhancing selectivity,[29] and hydrostability.[22] However, none of them revealed the mass transfer behavior and separation mechanism of such core–shell adsorbents. Thus, we would like to present a proof-of-concept experiment with a strong theoretical basis for material selection, a design criterion for selecting polymers to coat MOFs, and a simple transport equation through the core–shell structures.

We propose in this work a model and design criteria for core–shell adsorbents based on Fick's laws that may be used to guide future material selection for both enhancing stability and selectivity. We demonstrate through microscopy that electrospun fiber—MOF composites allow the material to be coated with nanoscale polymer films and verify that gas selectivity superior to both the individual polymer or MOF is observed over 3 min timescales using a composite fiber composed of a polyimide/poly(ethylene oxide) polymer blend and the MOF ZIF-8. ZIF-8 is used in this study because it has been extensively studied for its adsorption[43] and diffusion[44] characteristics, and these well-studied properties allow for better characterization of the impact of the fiber interface. Polyimide and poly(ethylene oxide) (PEO) blends have been used previously for separation of CO_2 from N_2 in membrane form, and are blended due to the contribution of strength from the glassy polyimide and the high selectivity of CO_2 over N_2 in PEO.[45] The polyimide used in this study is the commercially available Matrimid 5218, which is referred to simply as Matrimid (or MAT) hereafter. The diffusivity of both CO_2 and N_2 in ZIF-8 are around 2×10^{-8} and 4×10^{-8} cm^2/s, respectively; resulting in a slight kinetic selectivity towards N_2 at 35°C.[44] The diffusivity of each gas through MAT is around 100× lower than ZIF-8.[46] The diffusivity of CO_2 in PEO is around 10× less than ZIF-8, and the diffusivity of N_2 in PEO is around 100× less than ZIF-8.[45]

2 | MODELS AND THEORY

2.1 | Equilibrium separation of adsorbent

When adsorption occurs such that the adsorbent uptake quantity (Q) is sufficiently proportional to the pressure (***P***) or concentration (***C***), a linear isotherm may be used to represent the data given by:

$$Q = KP \text{ or } Q = K'C \tag{1}$$

where K or K' is Henry's constant or sorption coefficient. The uptake of a composite may be modeled as a function of the mole fraction (m_i) of each component if interfacial properties such as gaps or blockage are negligible:

$$Q = m_1 K_1 P + m_2 K_2 P \tag{2}$$

The selectivity of a preferred adsorbate a over a nonpreferential adsorbate b ($\alpha_{a/b}$) may also be found when comparing single-component isotherms of different gases at the same temperature. This is commonly performed using the ideal adsorbed solution theory (IAST), which, when all components may be described by a linear isotherm, reduces to[47]:

$$\alpha_{a,b} = \frac{K_a}{K_b}. \tag{3}$$

This is the selectivity when the system is allowed to reach thermodynamic equilibrium. Where α is the selectivity, K is the solubility, $\boldsymbol{D}$ is the diffusivity, a denotes the preferentially adsorbing gas, and b represents the nonpreferentially adsorbing gas.

2.2 | Kinetic separation of microporous adsorbent

Currently, the design of adsorbents to carry out adsorption-based separations with a kinetically selective mechanism is increasing.[41] These adsorbents may perform separations based on the differences in gas uptake rates. Using traditional single-component adsorbents by assuming D_a is greater than D_b, these materials have a maximum selectivity of[42]:

$$\alpha_{a,b} = \frac{K_a}{K_b}\sqrt{\frac{D_a}{D_b}}. \tag{4}$$

The uptake and selectivity of the separation then become a balancing act as the kinetic effects will eventually succumb to equilibrium selectivity (Equation (3)) as time increases.

2.3 | Kinetic separation of core–shell adsorbent

Fick's Laws of diffusion are commonly used to describe adsorption kinetics,[48] and may be expressed as:

$$J = -D\nabla C \tag{5}$$

$$\frac{\delta C}{\delta t} = -\nabla J \tag{6}$$

respectively, where J is the flux, C is the concentration and D is the diffusivity of the gas inside the adsorbent. For a two-dimensional (2D) core–shell system in which a shell of length L_S leads to a core of length L_C (Figure 1), the following boundary equations may be applied.

$$C = K_S C_0 \; x = 0, \; t > 0 \tag{7a}$$

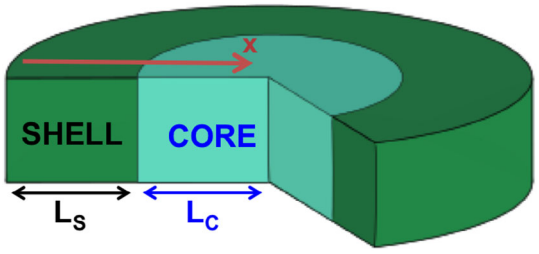

FIGURE 1 Two-dimensional geometry considered in the COMSOL FEM method where the green represents the shell of length L_S, and the blue represents a core of length L_C along the x-axis [Color figure can be viewed at wileyonlinelibrary.com]

$$C = 0,\ x > 0,\ t = 0 \tag{7b}$$

$$\frac{\delta C}{\delta t} = D_S \frac{\delta^2 C}{\delta x^2} 0 < x < LS \tag{7c}$$

$$\frac{\delta C}{\delta t} = D_C \frac{\delta^2 C}{\delta x^2} x > LS \tag{7d}$$

$$J = 0,\ x = L_S + L_C \tag{7e}$$

$$\mu_S = \mu_C x = L_S \tag{7f}$$

$$D_S \frac{\delta C}{\delta x}\bigg|_{L_S^-} = D_C \frac{\delta C}{\delta x}\bigg|_{L_S^+} \tag{7g}$$

where the last two terms express the continuity across the core–shell interface. μ_S and μ_C correspond to the chemical potential of the adsorbent in either phase and the final boundary condition bounds the continuity of flow through the interface.[49] These expressions state that the interface between the core and shell does not provide any additional influences to the transport of chemical species. K_S refers to Henry's constant of the shell, which is also commonly expressed as the solubility of the shell. With these equations, the assumptions of isothermal uptake, concentration-independent diffusion coefficients, and no gas–gas interactions inside the adsorbent are made. These simplifications are made so that a clear analytical expression could be derived by the end of this work that may be used to guide material design and expected phenomena.

Crank,[48] Barrer,[50] Jost,[49] and Carslaw[51] provide sets of particular solutions to some of these cases (described as laminates, heterogeneous adsorbents, or dual-phase adsorbents) with different sets of particular approximations. Furthermore, it is essential to develop predictive kinetic equations for the design of core–shell adsorbents. Therefore, we solve the diffusion equations for core–shell adsorbents using numerical methods and compare to a derived analytical model to describe the uptake equations for core–shell adsorbents. The total uptake at a particular time is found by solving Equation (6) at a particular $\boldsymbol{x}$ and integrating over time (Equation S1). COMSOL software was used to solve and illustrate the uptake of the core, the shell, and total adsorbent uptake as a function of time. These uptake curves are shown in Figure 2.

Three different regimes are observed in a dual-phase core–shell adsorbent: (a) exclusive shell uptake, (b) linear core uptake, and (c) asymptotic core uptake. There is an initial phase in which all of the uptake occurs in the shell, which may be defined as the lag-time ending at time φ. This is followed by a phase where uptake in the core (Q_c) may be approximated by a linear rate $\boldsymbol{\psi}$:

$$Q_C = \psi t + \varphi. \tag{8}$$

Following the linear uptake in the core is a nonlinear uptake region in which a maximum uptake is approached. The effects of changing L_C, L_S, D_C, and D_S on these uptake regimes are shown in Figures S1–S4). D_C has negligible influence as long as it is an order of magnitude larger than D_S. L_C primarily influences the length of linear uptake. Extending L_S or decreasing D_S increases both φ and linear uptake time while decreasing ψ.

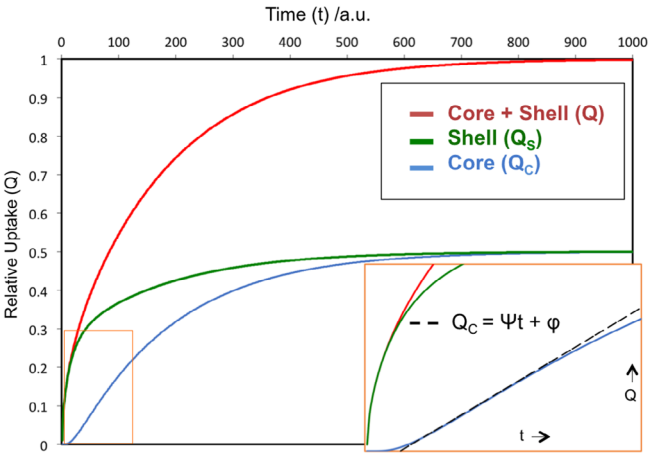

FIGURE 2 Example of uptake in a core–shell adsorbent generated in COMSOL where the red curve depicts the total uptake in the adsorbent, the green curve represents uptake exclusively in the shell, and the blue curve represents uptake exclusively in the core. The inset image is a zoomed-in region bounded by the orange rectangle, and the black dashed line is an extrapolation of the linear uptake region in the core [Color figure can be viewed at wileyonlinelibrary.com]

By manipulating the contribution of the shell uptake and core uptake along with influences of the uptake phase, the selectivity may be manipulated. A plot of selectivity versus adsorption time is presented by assuming a diffusivity ratio of 10 for two species diffusing through the shell, in which the effects of both shell thickness and adsorption time on the selectivity are demonstrated (Figure 3).

Three selectivity limits may be seen from these plots, with one corresponding to dominance of each different uptake phase. When the shell has the same uptake capacity as the core, diffusion into the shell dominates selectivity. This selectivity has the limit of a single-phase adsorbent kinetic separation, given by Equation (4).[42]

When the shell becomes negligibly small, the steady-state uptake by the core reservoir dominates the selectivity, where the $\boldsymbol{\psi}$ dictates the uptake rate, and selectivity approaches the ratio of these two slopes (called permeation selectivity):

$$\alpha_{a,b} = \frac{\gamma_a}{\gamma_b} = \frac{D_a}{D_b}\frac{K_a}{K_b} \tag{9}$$

This observed permeation selectivity is notable since it has not been reported for cyclic adsorption-based separations, yet this model clearly shows that this regime is accessible. A more rigorous justification for the existence of this permeation selectivity is given in the Supporting Information after the derivation of the analytical model given later in the text. After this initial spike in selectivity, the gases start to approach their maximum equilibrium values and the final

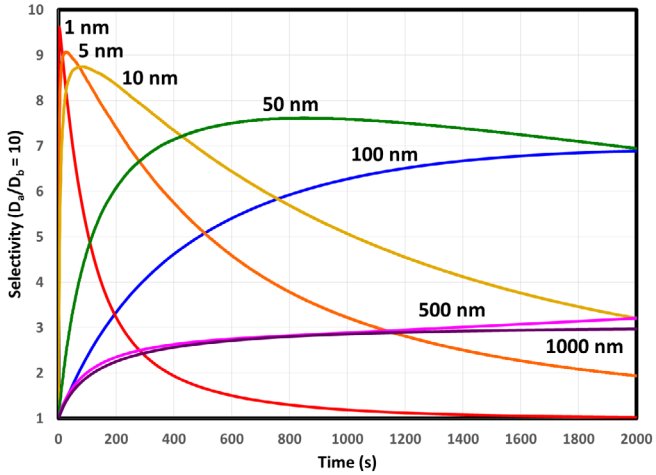

FIGURE 3 Selectivity as a function of time calculated in COMSOL for two gases with a D/D ratio of 10 in the shell. Each curve represents a different shell length (L_S = 1 [red], 5 [orange], 10 [yellow], 50 [green], 100 [blue], 500 [indigo], and 1,000 [violet]. The diffusivity of gas a in the shell ($D_{S,\,a}$) is 1×10^{-16} cm^2/s and the diffusivity of gas b in the shell ($D_{S,b}$) is 1×10^{-17}. All other values are held constant for each test: L_{CORE} = 5,000 nm, C_0 = 1 mol/m^3, $D_C = 1 \times 10^{-10}$ cm^2/s [Color figure can be viewed at wileyonlinelibrary.com]

uptake phase dominates, the selectivity eventually approaches the thermodynamic selectivity given by Equation (3).

2.4 | Kinetics with analytical solution

From these finite-element method (FEM) simulations, we see that if $D_C/D_S > 10$, that D_C has a negligible effect on the uptake because the adsorbing gas is able to approach an equilibrium value in the core much faster than it is able to pass into the core from the shell (Figure S1): allowing us to consider a boundary condition in which the core is considered to be well-mixed at all times by dropping Equations (7d–7f) and replacing with Equation (S6). Since the motivation behind this work is to use the shell as a selective layer and the core as a reservoir, selecting a core material with much faster diffusivities than the shell may be expected. Therefore, if we are able to neglect the diffusivity in the core, we may instead model the core as a reservoir of capacity Q_c that maintains equal concentration throughout, allowing for an analytical solution that parallels work by Paul and DiBenedetto,[52] by using an adsorbent instead of a reservoir and a more generalized integration. The full analytical solutions are provided in the Supporting Information, and the important results are presented here.

The uptake of a core–shell adsorbent is given as:

$$Q = A{\cdot}P{\cdot}K_S{\cdot}L_S\left[1 - \frac{x}{L_S} + \frac{1}{\eta} - \sum_n \frac{2\left(\beta_n^2+\eta^2\right)\cos\left(\beta_n \frac{x}{L_S}\right)}{\beta_n^2\left(\beta_n^2+\eta^2+\eta\right)} e^{\frac{-D_S\beta_n^2 t}{L_S^2}}\right] \tag{10}$$

where A is the surface area of the shell, the β_n values represent the non-negative roots of the equation $\beta\tan(\beta) = \eta$ and

$$\eta = \frac{K_S}{K_C}\frac{A{\cdot}L_S}{V_C} = \frac{Q_{\infty,S}}{Q_{\infty,C}} \tag{11}$$

where $Q_{\infty,S}$ is the maximum capacity of the shell and $Q_{\infty,C}$ is the maximum capacity of the core. The total uptake, Q, is calculated when setting x = 0, resulting in the cosine expression in Equation (8) going to one. The uptake in the core (Q_c) is solved by setting $x = L_S$. A model exclusively for Q_c is important for defining the uptake regimes (a–c), which subsequently allows the definition of design criteria for stability and selectivity. Figure S5 demonstrates that this analytical solution nearly matches the corresponding finite-element model uptake curve when the D_C/D_S ratio is 10.

The lag phase (φ) separating uptake Phase (i) from Phase (ii) may be approximated as[50]:

$$\varphi = \frac{L_S^2}{6D_S}. \tag{12}$$

A different solution to this time-lag method in which the six in the denominator is replaced by a more complex term as a function of η is provided in the Supporting Information (Equation (S13)). This correction is important for calculating the D_S explicitly from the linear uptake region since it is an extrapolation from the slope, which is a function of these parameters. However, when using this approximation for the time until core penetration, the downstream Q_C has no impact on the true **φ** and is considered unimportant, as demonstrated in Figure S4.

After the lag phase, the summation term in Equation (10) will become negligible, and **ψ** from Equation (8) is expressed as[52]:

$$\begin{aligned}\Psi &= \frac{A{\cdot}P{\cdot}K_S{\cdot}D_S}{L_S}\left[\frac{2\left(\beta_0^2+\eta^2\right)\cos\cos\left(\beta_0\right)}{\left(\beta_0^2+\eta^2+\eta\right)} e^{\frac{-D_S\beta_0^2 t}{L_S^2}}\right] \\ &= \frac{A{\cdot}P{\cdot}K_S{\cdot}L_S}{6\varphi}\left[\frac{2\left(\beta_0^2+\eta^2\right)\cos\cos\left(\beta_0\right)}{\left(\beta_0^2+\eta^2+\eta\right)} e^{\frac{-\beta_0^2 t}{6\varphi}}\right]\end{aligned} \tag{13}$$

Where β_0 is the first non-negative root of $\beta tan\beta = \eta$. This term is linear when the term in the exponential is near zero, and we may define uptake region (b) to occur after φ and before this exponential term influences Ψ. As an approximation, it may be assumed that the function e^{-x} is linear until the exponential term x surpasses a value of 0.25 (however, this term may be adjusted for desired tolerance). We may then define region (b) as occurring from:

$$\varphi < t_{\text{Linear Uptake (ii)}} < \frac{6\varphi}{4\beta_0^2} \tag{14}$$

This criterion allows for the design of an adsorbent for the time regimes. When designed properly, the undesirable species should be the slower adsorbing species, and the desirable adsorbing species the faster one. When undesirable adsorbates are in Phase (i) protection occurs, when both adsorbates are in Phase (ii) maximum relative selectivity occurs, and when a desirable adsorbate is in Phase (iii) maximum

relative uptake occurs. Designing systems for maximum relative selectivity is recommended for purification processes where multiple passes may be considered. Designing systems for maximum relative uptake are recommended for systems where purity is less important than the total uptake.

In sum, this simulation study and analytical model demonstrate that two major uptake advantages of using this dual-adsorbent scheme with electrospun fibers may be expected: (a) The thin polymer coating covering the MOF particles enabled by electrospinning could be used to increase kinetic selectivity; (b) The kinetic bottle-necking of the polymer layer both dictates the time until a fluid reaches the adsorbent through the characteristic lag-time and rate in which the adsorbent fills. Increasing the lag-time before uptake by the particle is of particular importance if the polymer layer is being designed to block fluids from the core that will poison the adsorbent such as water or sour gas over the time-scale of an absorption cycle; enhanced protection and adsorbent lifetime could be expected.

In the following sections, we aim to experimentally confirm that thin polymer layers are indeed wrapping particles embedded in these electrospun fibers with nano-scale coatings, and that enhanced selectivity can be observed relative to either the core or shell components individually as predicted by our theoretical derivations.

3 | EXPERIMENTAL MATERIALS AND METHODS

3.1 | Material preparation

Matrimid 5218 (MAT, M_w 80,000)[53] was provided by Huntsman; poly(ethylene oxide) (PEO, M_v 400,000), zinc nitrate ($Zn[NO_3]_2$, purity 98%), 2-methyl immidazolate ($CH_3C_3H_2NH$, purity 99%), and methanol (CH_2OH, 99.8%) were purchased from Sigma-Aldrich; carbon dioxide (CO_2), nitrogen (N_2), and helium (He) were purchased from Praxair each at ultra-high purity grade. ZIF-8 was synthesized using Cravillon's method[54] as described previously.[35] Two electrospinning suspensions were prepared. Each was composed of a 100 mg MAT and 100 mg PEO dissolved in 10 ml of dichloromethane. The first had 50 mg ZIF-8 suspended in solution (for a 20% ZIF-8 composite, called 1:1:0.5 MAT:PEO:ZIF-8 fibers), and the second had 200 mg ZIF-8 suspended in solution (for a 50% ZIF-8 composite, called 1:1:2 MAT:PEO:ZIF-8 fibers). Electrospun fibers were fabricated using an apparatus described previously.[34] 1:1:0.25 MAT:PEO:ZIF-8 and 1:1:2 MAT:PEO:ZIF-8 were prepared in a previous study by the same manner and more details and characterization are shown there.[35]

3.2 | Microscopy

Scanning electron microscopy (SEM) was performed on a Zeiss EVO MA10 microscope with a tungsten thermionic electron gun at an accelerating voltage of 18 kV. Transmission Electron Microscopy (TEM) was performed on a CM-200-FEG microscope at an accelerating voltage of 200 kV. Scanning transmission electron microscopy (STEM) was performed on a Titan Krios microscope under low-dose mode at 200 kV using a high angle annular dark field detector (HAADF). Tomography was done along two perpendicular tilt axis each containing 89 images each from −55° to 55° spaced with the Saxton scheme. Tomograms were constructed and processed using IMOD software provided by the University of Colorado Boulder, and model was developed with FEI Avizo software from this tomogram using techniques from literature for nanoparticle reconstruction.[55]

3.3 | Adsorption studies

Adsorption experiments were performed on a Quantachrome iSorb HP2 machine. Helium void fractions were taken before each measurement. Default equations of state recommended by Quantachrome software were used for each gas: Helmholtz for CO_2 and N_2, and the mBWR-Jacobsen for He. A maximum equilibrium for CO_2 and N_2 was set to 3 min. Initial activation was performed at 55°C for 72 hr under vacuum, and activation between each run was performed at 55°C for 12 hr under vacuum.

4 | RESULTS AND DISCUSSION

4.1 | Materials

Images of the four materials tested in the adsorption tests are shown in Figure 4 including SEM images of ZIF-8 powder, pure 1:1 MAT:PEO fibers, and the composite 1:1:0.5 and 1:1:2 MAT:PEO:ZIF-8 fibers. TEM images of the composite fibers are also shown to demonstrate the internal morphology in Figure 5.

From these images, it may be seen that the 1:1 MAT:PEO fibers and 1:1:0.5 MAT:PEO:ZIF-8 fibers are of similar diameters, but the 1:1:2 fibers are smaller. All fibers are larger than the average 200 nm ZIF-8 particle size. ZIF-8 is seen embedded throughout the composite fibers in Figure 5, however, the 2D projection of these fibers does not accurately demonstrate how far from the surface these particles are. For this reason, a tomogram was constructed over a segment of the 1:1:2 MAT:PEO:ZIF-8 fibers to understand how these particles load (Figure 6).

From the 3D TEM imaging, we are able to measure the distance between the particle and the surface of the fiber where the polymer appears to extend out to wrap the particle. The thickness of the region between MOF and fiber surface is measured to reach minimums on the order of 10 nm. Videos of the TEM images used to construct these models and of different views of the model are given in the Supporting Information.

4.2 | Adsorption isotherms and availability

In literature, multiple reports show isotherms of polymer-coated MOFs in which isotherms demonstrate the expected shape with lower uptakes for some gases when gases such as nitrogen diffuse through the polymer slower than the allowed equilibrium time.[22,29,30] The resulting isotherm demonstrates that the selectivity based on a combined diffusivity and solubility factors as long as diffusivity is

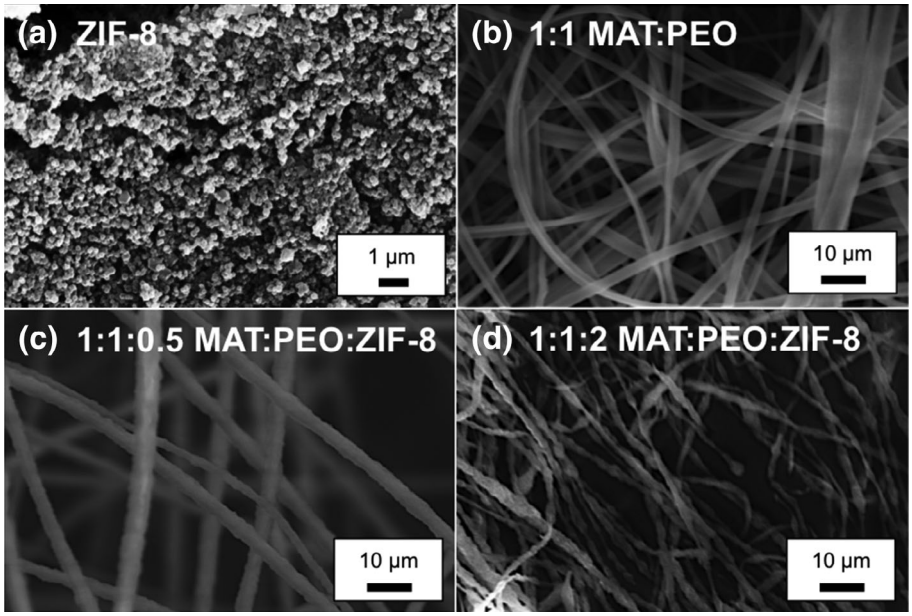

FIGURE 4 SEM image of (a) pure ZIF-8 powder, (b) 1:1 Matrimid:PEO, (c) 1:1:0.5 MAT:PEO:ZIF-8, and (d) 1:1:2 MAT:PEO:ZIF-8

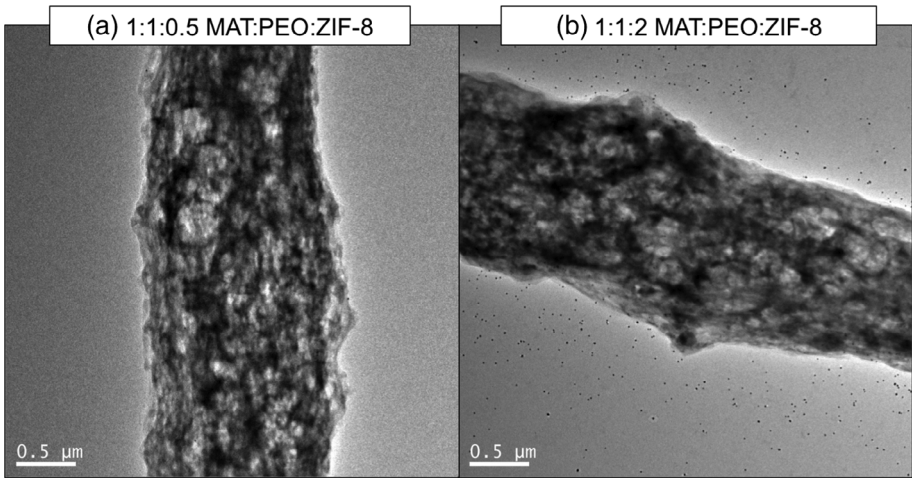

FIGURE 5 TEM image of (a) 1:1:0.5 MAT:PEO:ZIF-8 fibers and (b) 1:1:2 MAT:PEO:ZIF-8 fibers

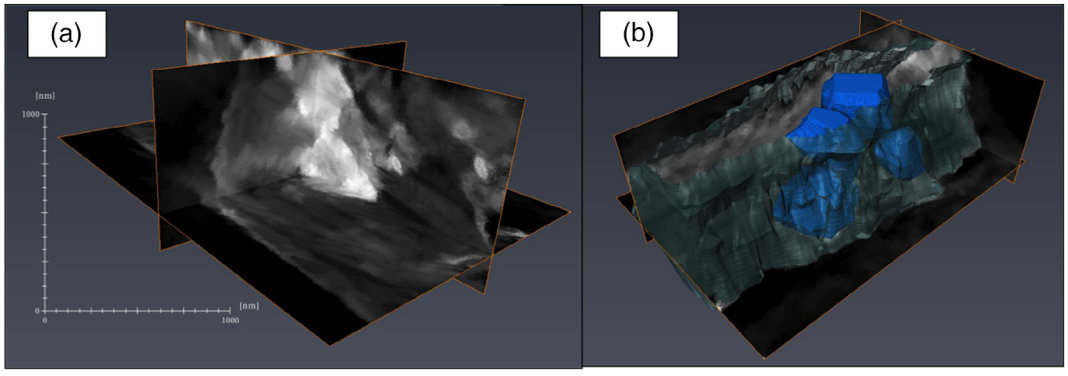

FIGURE 6 Tomogram and model constructed from series of HAADF TEM images of 1:1:0.5 MAT:PEO:ZIF-8 fibers over two tilt angles. (a) Three representative slices of the tomogram in each plane where the bright areas represent ZIF-8 and the grey areas represent fiber. The scale

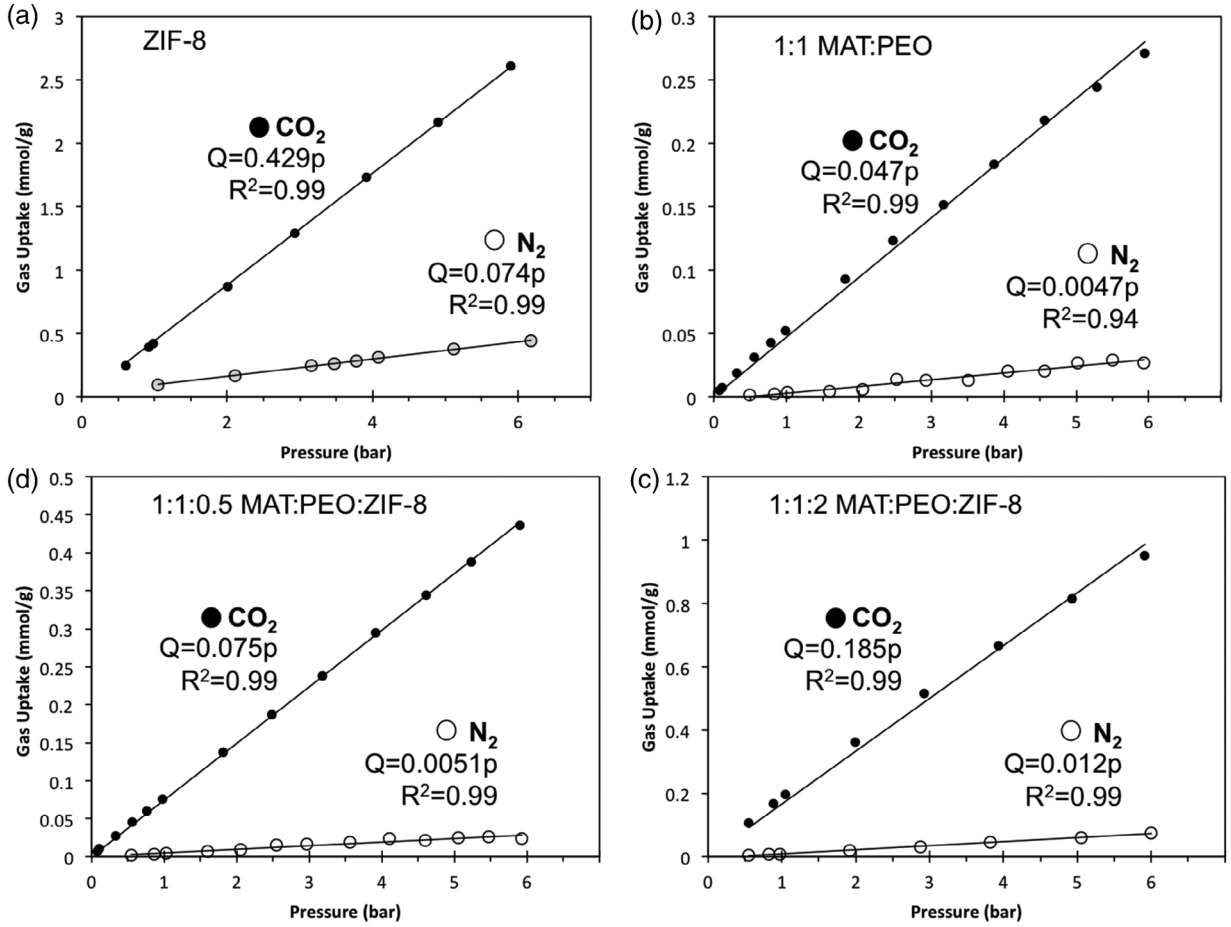

FIGURE 7 Kinetically suppressed isotherms for (a) ZIF-8, (b) 1:1 MAT:PEO fibers, (c) 1:1:2 MAT:PEO:ZIF-8 fibers, and (d) 1:1:0.5 MAT:PEO:ZIF-8 fibers with a maximum of 3 min equilibrium time up to 6 bar pressure of either CO_2 or N_2

sufficiently independent of concentration and the adsorption during dosing time does not exceed the uptake value of the next point. This method is used here. Isotherms were collected at 45°C for each material with both CO_2 and N_2 up to 6 bar with a predefined maximum equilibrium time of 3 min. Three minutes was chosen as the short equilibrium time since it falls within the typical optimum 100–200 s between vacuum swings during vacuum adsorption cycles as calculated by Susarla and coworkers.[56] These isotherms are shown in Figure 7 along with their linear fit.

In the range of pressures tested, each isotherm appears sufficiently straight and is fit to a linear isotherm (Equation (1)) with a strong correlation coefficient. The linear nature of the isotherms for pure ZIF-8 and the 1:1 MAT:PEO fibers are near those found in the literature for CO_2 and N_2. ZIF-8 CO_2 isotherms are found to be linear until around 10 bar, where they begin to flatten due to pore filling, whereas N_2 isotherms appear linear up to at least 25 bar.[57] PEO appears to follow a linear isotherm up to 10 bar, where it begins to follow a convex path following a Flory-Huggins isotherm, whereas the nitrogen isotherm appears linear up to 20 bar.[45] MAT isotherms have concave isotherms for both N_2 and CO_2 which have been fit to dual-site polymeric isotherms.[58] N_2 isotherms in MAT become nonlinear at around 5 bar and CO_2 isotherms become nonlinear around 2 bar.

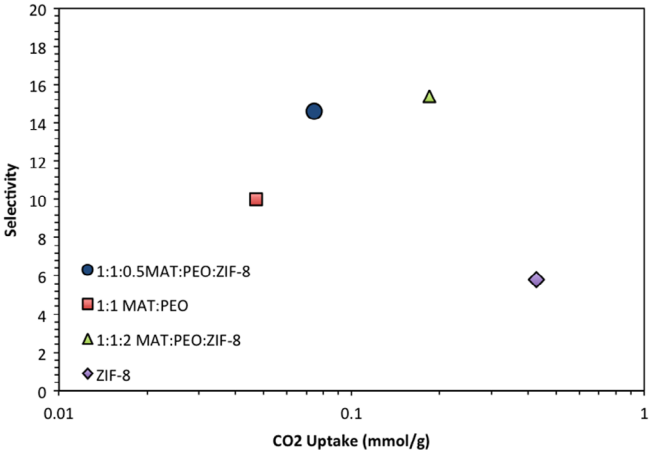

FIGURE 8 CO_2/N_2 selectivity plotted against CO_2 uptake for 1:1 MAT:PEO fibers (red square), 1:1:0.5 MAT:PEO:ZIF-8 fibers (blue circle), 1:1:2 MAT:PEO:ZIF-8 fibers (green triangle), and ZIF-8 (purple diamond) [Color figure can be viewed at wileyonlinelibrary.com]

The CO_2 uptake at 1 bar (calculated as *S*) for each material plotted against the α_{CO_2/N_2} can be found in Figure 8. The measured ZIF-8 selectivity at 3 min of equilibration match well with results for fully equilibrated isotherms in literature, where ZIF-8 experimental

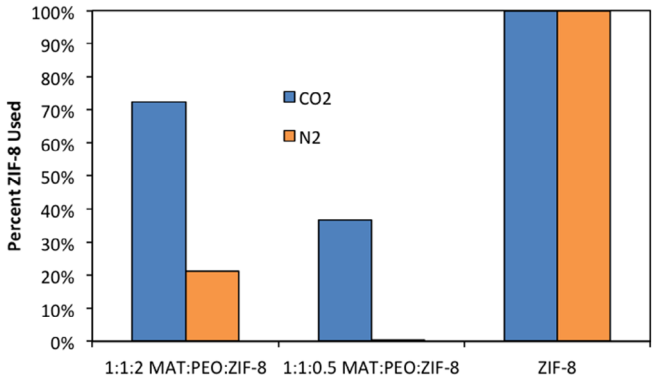

FIGURE 9 Histogram of approximate percentage ZIF-8 capacity used for CO_2 uptake (blue) and N_2 uptake (orange) for each ZIF-8 containing material studied over the 3 min time-step adsorption tests [Color figure can be viewed at wileyonlinelibrary.com]

selectivity is between 5 and 6 and CO_2 uptake near 45°C and 1 bar is 0.45 mmol/g.[59] This is expected for ZIF-8 under 500 nm diameter at these conditions since, with diffusivities of 2×10^{-8} and 3×10^{-8} cm^2/s for CO_2 and N_2, respectively, uptake was found to be too rapid for experimental measurements with traditional techniques at 35°C,[44] and may be expected to be even faster at 45°C.[48] Also, a noteworthy fact is that N_2 diffuses through ZIF-8 faster than CO_2, so any kinetic separations with pure ZIF-8 would result in a lower selectivity than the equilibrium state. Both pure CO_2 and N_2 isotherms for MAT and PEO isotherms found in literature are of the same order of magnitude as those found for the 1:1 MAT:PEO fibers,[45,58] suggesting that uptake is observed in both the MAT and PEO portions of the fibers, and nearly complete uptake is reached over the 3 min equilibrium time.

The MOF-embedded fibers both show an excess selectivity compared to either the pure MOF powder or the 1:1 MAT:PEO fibers. In both cases, a larger percentage of the embedded ZIF-8 is used for CO_2 uptake at 3 min over N_2 (Figure 9); as predicted by the models presented in section 2. The ZIF-8 used in the 1:1:2 fibers is larger than in the 1:1:0.5 fibers for each gas. This is likely because those fibers have a smaller diameter and also may contain ZIF-8 to ZIF-8 passages inside the fiber as well-resulting in a statistically thinner polymer coating than in the 1:1:0.5 fibers. The percentage of ZIF-8 used was approximated by assuming nearly complete uptake in the polymer fiber and dividing the resulting uptake by the full ZIF-8 uptake at the weight percent of ZIF-8 in the fibers.

5 | CONCLUSION

We present in this work an analytical model to describe the uptake in a core–shell adsorbent that is shown to match the uptake predicted by a finite element model well under the condition that the diffusivity in the core is at least an order of magnitude larger than the diffusivity of the shell. This model shows that kinetic selectivity greater than that predicted from the classical kinetic separation model based on the microporous adsorbents are accessible to core–shell adsorbents and that permeation selectivity may be realized. Three different uptake regimes that could be controlled by material design and uptake times—(a) exclusive shell uptake, (b) linear core uptake, and (c) asymptotic core uptake—are presented and the tradeoffs between protection, productivity, and selectivity between these regimes are discussed. The proof-of-concept experiments were carried out on electrospun MOF–polymer composites. A microscopy study showing that thin polymer coatings over MOF materials can be made through the electrospinning process that could maximize the optimum selectivity regime, and adsorption studies were performed to demonstrate that selectivity/uptake combinations unobtainable by either core or shell alone can be realized. This work is expected to be vital for guiding future core–shell adsorbents design.

ACKNOWLEDGMENTS

This research work was financially supported by Arizona State University and the National Science Foundation (Grant Number CBET-1748641 and CMMI-1825594). The authors gratefully acknowledge the use of the Leroy Eyring Center for Solid State Science at Arizona State University, and in particular the phenomenal support of Dewight Williams with tomography. The authors are also indebted to the equipment support provided by SEMTE lab manager Fred Pena.

NOTATION

A	surface area of shell, m^2
C	concentration, mol/m^3
C_0	initial concentration, mol/m^3
D	diffusivity, cm^2/s
D_S	diffusivity in shell
D_C	diffusivity in core
J	flux, $mmol/(m^2 \cdot s)$
K	Henry's constant
L	length for diffusion, nm
L_S	length of shell, nm
L_C	length of core, nm
m	mole fraction
P	pressure, Pa
Q	adsorption uptake, mmol/g
T	temperature, K
t	time, s
V_C	volume of core, m^3
x	diffusion distance, nm
α	selectivity
μ	chemical potential
μ_S	chemical potential of adsorbent in shell
μ_C	chemical potential of adsorbent in core
ψ	adsorption uptake rate, $mmol/(g \cdot s)$
φ	fitting parameter

ORCID

Bohan Shan https://orcid.org/0000-0001-5674-981X
Bin Mu https://orcid.org/0000-0002-9117-1299

REFERENCES

1. Hoskins BF, Robson R. Infinite polymeric frameworks consisting of three dimensionally linked rod-like segments. *J Am Chem Soc*. 1989; 111:5962-5964.
2. Chen Y, Shan B, Yang C, et al. Environmentally friendly synthesis of flexible MOFs M(NA) 2 (M = Zn, Co, Cu, Cd) with large and regenerable ammonia capacity. *J Mater Chem A*. 2018;6:9922-9929.
3. Shan B, Yu J, Armstrong MR, et al. A cobalt metal-organic framework with small pore size for adsorptive separation of CO_2 over N_2 and CH_4. *AIChE J*. 2017;63:4532-4540.
4. Armstrong MR, Shan B, Cheng Z, et al. Adsorption and diffusion of carbon dioxide on the metal-organic framework CuBTB. *Chem Eng Sci*. 2017;167:10-17.
5. Mu B, Li F, Walton KS. A novel metal–organic coordination polymer for selective adsorption of CO_2 over CH_4. *Chem Commun*. 2009;18: 2493-2495. https://doi.org/10.1039/b819828d.
6. McIntyre SM, Shan B, Wang R, et al. Monte Carlo simulations to examine the role of pore structure on ambient air separation in metal–organic frameworks. *Ind Eng Chem Res*. 2018;57:9240-9253.
7. Armstrong MR, Senthilnathan S, Balzer CJ, et al. Particle size studies to reveal crystallization mechanisms of the metal organic framework HKUST-1 during sonochemical synthesis. *Ultrason Sonochem*. 2017; 34:365-370.
8. Trager R. MOFs offer safer toxic gas storage. *Chemistry World*; 2016. https://www.chemistryworld.com/news/mofs-offer-safer-toxic-gas-storage-/1017610.article.
9. Vaughan O. Porous by design. *Nature*. 2014;511:19. https://doi.org/10.1038/nature13371.
10. Burtch NC, Jasuja H, Walton KS. Water stability and adsorption in metal-organic frameworks. *Chem Rev*. 2014;114:10575-10612.
11. Li N, Xu J, Feng R, Hu T-L, Bu X-H. Governing metal–organic frameworks towards high stability. *Chem Commun*. 2016;52:8501-8513.
12. Yuan S, Qin J-S, Lollar CT, Zhou H-C. Stable metal-organic frameworks with group 4 metals: current status and trends. *ACS Cent Sci*. 2018;4:440-450.
13. Yuan S, Feng L, Wang K, et al. Stable metal-organic frameworks: design, synthesis, and applications. *Adv Mater*. 2018;30:1704303.
14. Drage TC, Snape CE, Stevens LA, et al. Materials challenges for the development of solid sorbents for post-combustion carbon capture. *J Mater Chem*. 2012;22:2815-2823. https://doi.org/10.1039/c2jm12592g.
15. Geng J-C, Xue D-M, Liu X-Q, Shi Y-Q, Sun L-B. N-doped porous carbons for CO_2 capture: rational choice of N-containing polymer with high phenyl density as precursor. *AIChE J*. 2017;63:1648-1658.
16. Sun L-B, Kang Y-H, Shi Y-Q, Jiang Y, Liu X-Q. Highly selective capture of the greenhouse gas CO_2 in polymers. *ACS Sustain Chem Eng*. 2015; 3:3077-3085.
17. Jiang Y, Tan P, Qi S-C, et al. Metal-organic frameworks with target-specific active sites switched by photoresponsive motifs: efficient adsorbents for tailorable CO_2 capture. *Angew Chem Int Ed*. 2019;58: 6600-6604.
18. Patel HA, Byun J, Yavuz CT. Carbon dioxide capture adsorbents: chemistry and methods. *ChemSusChem*. 2017;10:1303-1317.
19. Bao Z, Yu L, Ren Q, Lu X, Deng S. Adsorption of CO 2 and CH_4 on a magnesium-based metal organic framework. *J Colloid Interface Sci*. 2011;353:549-556.
20. Li T, Sullivan JE, Rosi NL. Design and preparation of a core–shell metal–organic framework for selective CO_2 capture. *J Am Chem Soc*. 2013;135:9984-9987.
21. Hirai K, Furukawa S, Kondo M, Uehara H, Sakata O, Kitagawa S. Sequential functionalization of porous coordination polymer crystals. *Angew Chem Int Ed*. 2011;50:8057-8061.
22. Carné-Sánchez A, Stylianou KC, Carbonell C, Naderi M, Imaz I, Maspoch D. Protecting metal-organic framework crystals from hydrolytic degradation by spray-dry encapsulating them into polystyrene microspheres. *Adv Mater*. 2015;27:869-873.
23. Qian X, Sun F, Sun J, et al. Imparting surface hydrophobicity to metal–organic frameworks using a facile solution-immersion process to enhance water stability for CO_2 capture. *Nanoscale*. 2017;9:2003-2008.
24. Zhang W, Hu Y, Ge J, Jiang H, Yu S. A facile and general coating approach to moisture/water-resistant metal–organic frameworks with intact porosity. *J Am Chem Soc*. 2014;136:16978-16981.
25. Liu D, Huxford RC, Lin W. Phosphorescent nanoscale coordination polymers as contrast agents for optical imaging. *Angew Chem Int Ed*. 2011;50:3696-3700.
26. Liu X, Li Y, Ban Y, et al. Improvement of hydrothermal stability of zeolitic imidazolate frameworks. *Chem Commun*. 2013;49:9140.
27. Yang SJ, Park CR. Preparation of highly moisture-resistant black-colored metal organic frameworks. *Adv Mater*. 2012;24:4010-4013.
28. Rose M, Boehringer B, Jolly M, Fischer R, Kaskel S. MOF processing by electrospinning for functional textiles. *Adv Eng Mater*. 2011;13: 356-360.
29. Ostermann R, Cravillon J, Weidmann C, Wiebcke M, Smarsly BM. Metal–organic framework nanofibers viaelectrospinning. *Chem Commun*. 2011;47:442-444.
30. Armstrong M, Balzer C, Shan B, Mu B. Influence of particle size and loading on particle accessibility in electrospun poly(ethylene oxide) and ZIF-8 composite fibers: experiments and theory. *Langmuir*. 2017; 33:9066-9072.
31. Armstrong M, Sirous P, Shan B, et al. Prolonged HKUST-1 functionality under extreme hydrothermal conditions by electrospinning polystyrene fibers as a new coating method. *Microporous Mesoporous Mater*. 2018;270:34-39.
32. Balzer C, Armstrong M, Shan B, et al. Modeling nanoparticle dispersion in electrospun nanofibers. *Langmuir*. 2018;34:1340-1346.
33. Armstrong MR, Shan B, Mu B. Microscopy study of morphology of electrospun Fiber-MOF composites with secondary growth. *MRS Adv*. 2017;2:2457-2463.
34. Armstrong MR, Yuriar Arredondo KY, Liu C-Y, et al. UiO-66 MOF and poly(vinyl cinnamate) nanofiber composite membranes synthesized by a facile three-stage process. *Ind Eng Chem Res*. 2015;54:12386-12392.
35. Armstrong MR, Shan B, Maringanti SV, Zheng W, Mu B. Hierarchical pore structures and high ZIF-8 loading on Matrimid electrospun fibers by additive removal from a blended polymer precursor. *Ind Eng Chem Res*. 2016;55:9944-9951.
36. Ko FK, Wan Y. *Introduction to nanofiber materials*. Cambridge, MA: Cambridge University Press; 2014.
37. Schreiner C, Bridge AT, Hunley MT, Long TE, Green MD. Segmented imidazolium ionenes: solution rheology, thermomechanical properties, and electrospinning. *Polymer (Guildf)*. 2017;114:257-265.
38. Elsabee MZ, Naguib HF, Morsi RE. Chitosan based nanofibers, review. *Mater Sci Eng C*. 2012;32:1711-1726.
39. Tipduangta P, Belton P, Fábián L, et al. Electrospun polymer blend nanofibers for tunable drug delivery: the role of transformative phase separation on controlling the release rate. *Mol Pharm*. 2016;13:25-39.
40. Joshi MK, Tiwari AP, Pant HR, et al. In situ generation of cellulose nanocrystals in Polycaprolactone nanofibers: effects on crystallinity, mechanical strength, biocompatibility, and biomimetic mineralization. *ACS Appl Mater Interfaces*. 2015;7:19672-19683.
41. Wang Y, Zhao D. Beyond equilibrium: metal–organic frameworks for molecular sieving and kinetic gas separation. *Cryst Growth Des*. 2017; 17:2291-2308.
42. Ruthven DM, Reyes SC. Adsorptive separation of light olefins from paraffins. *Microporous Mesoporous Mater*. 2007;104:59-66.
43. Zhang C, Koros WJ. Zeolitic Imidazolate framework-enabled membranes: challenges and opportunities. *J Phys Chem Lett*. 2015;6:3841-3849.

44. Zhang C, Lively RP, Zhang K, et al. Unexpected molecular sieving properties of Zeolitic Imidazolate Framework-8. *J Phys Chem Lett*. 2012;3:2130-2134.
45. Lin H, Freeman BD. Gas solubility, diffusivity and permeability in poly(ethylene oxide). *J Membr Sci*. 2004;239:105-117.
46. Li X, Wang M, Wang S, et al. Constructing CO_2 transport passageways in Matrimid® membranes using nanohydrogels for efficient carbon capture. *J Membr Sci*. 2015;474:156-166.
47. Walton KS, Sholl DS. Predicting multicomponent adsorption: 50 years of the ideal adsorbed solution theory. *AIChE J*. 2015;61:2757-2762.
48. Crank J. *The mathematics of diffusion*. Oxford: Oxford University Press; 1975.
49. Jost W. *Diffusion in solids, liquids and gases*. New York: Academic Press Inc; 1952.
50. Barrer RM. Diffusion and permeation in heterogeneous media. In: Crank J, Park GS, eds. *Diffusion in Polymers*. New York: Academic Press Inc.; 1968:165-217.
51. Carslaw HS, Jaeger JC. *Heat conduction in solids*. Oxford: Oxford University Press; 1959.
52. Paul DR, DiBenedetto AT. Diffusion in amorphous polymers. *J Polym Sci Part C*. 1965;10:17-44.
53. Chimica I, Dicma A, Studiorum-universita AM. Vapor and liquid sorption in Matrimid polyimide: experimental characterization and modeling. *Ind Eng Chem Res*. 2013;52:8936-8945.
54. Cravillon J, Nayuk R, Springer S, et al. Controlling Zeolitic Imidazolate framework nano- and microcrystal formation: insight into crystal growth by time-resolved in situ static light scattering. *Chem Mater*. 2011;23:2130-2141.
55. Ersen O, Florea I, Hirlimann C. Exploring nanomaterials with 3D electron microscopy. *Biochem Pharmacol*. 2015;18:395-408.
56. Rajendran A, Soon L, Tan C, Sue J, Lim T. Energy and cost estimates for capturing CO_2 from a dry flue gas using pressure/vacuum swing adsorption. *Chem Eng Res des*. 2015;102:354-367.
57. Zhang Z, Xian S, Xia Q, et al. Enhancement of CO_2 adsorption and CO_2/N_2 selectivity on ZIF-8 via postsynthetic modification. *AIChE J*. 2013;59:2195-2206.
58. Scholes CA, Tao WX, Stevens GW, Kentish SE. Sorption of methane, nitrogen, carbon dioxide, and water in Matrimid 5218. *J Appl Polym Sci*. 2010;117:2284-2289.
59. Huang H, Zhang W, Liu D, et al. Effect of temperature on gas adsorption and separation in ZIF-8: a combined experimental and molecular simulation study. *Chem Eng Sci*. 2011;66:6297-6305.

SUPPORTING INFORMATION

Additional supporting information may be found online in the Supporting Information section at the end of this article.

How to cite this article: Armstrong MR, Shan B, Winarta J, Mu B. Core–shell adsorbents by electrospun MOF-polymer composites with improved adsorption properties: Theory and experiments. *AIChE J*. 2020;66:e16816. https://doi.org/10.1002/aic.16816